

Numerical investigation of the effect of different parameters on emitted shockwave from bubble collapse in a nozzle

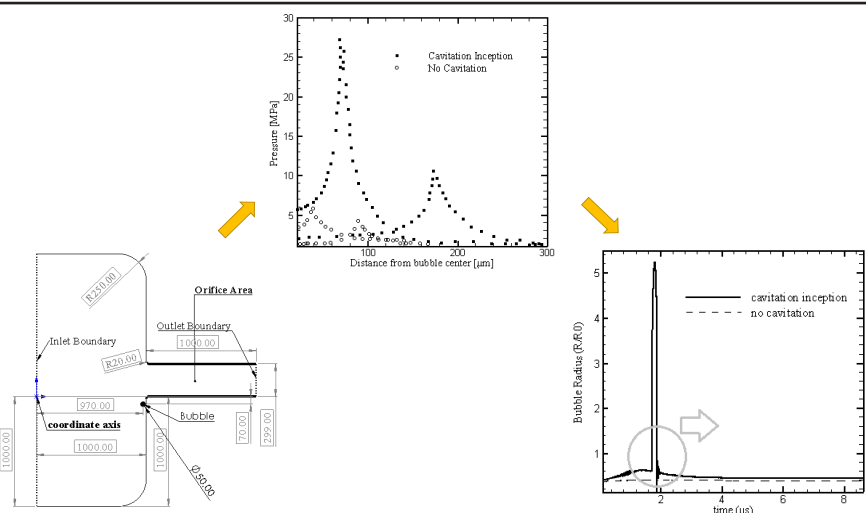
Seyed Mohammad Javad Zeidi, Miralam Mahdi*

Department of Mechanical Engineering, Shahid Rajaee Teacher Training University, Tehran, Iran

HIGHLIGHTS

- An Eulerian/Lagrangian approach using Reynolds average Navier-Stokes (RANS) and bubble dynamic equations are used for the prediction of cavitation inception.
- The modified form of critical pressure which was introduced by Singhal et al. is also used for evaluating critical pressure as cavitation starts.
- Increasing pressure difference can severely increase shockwave, while increasing initial radius will decrease the amount of emitted shockwave.
- Effects of surface tension, dynamic viscosity, and liquid density on bubble dynamic are evaluated.

GRAPHICAL ABSTRACT



ARTICLE INFO

Article history:

Received 11 November 2020

Revised 24 April 2021

Accepted 24 April 2021

Keywords:

Cavitation

Shockwave

Eulerian/Lagrangian approach

Nozzle

ABSTRACT

Cavitation can be extremely beneficial for the first spray breakup and to enhance atomization quality. An Eulerian/Lagrangian approach using Reynolds average Navier-Stokes (RANS) and bubble dynamic equations was used for the prediction of cavitation inception. A comprehensive validation was also performed using the Eulerian and Lagrangian equations in the current numerical approach. First, the carrying liquid was simulated by the finite volume method in order to obtain pressure and velocity in the whole computational domain, and a one-way coupling between the Eulerian and Lagrangian parts was used. The Reynolds stress transport model (RSTM) was used for calculating turbulent parameters, and the continuous filter white noise (CFWN) model was used for modeling fluctuating terms of velocity. Rayleigh-Plesset and a modified form of the bubble motion equation were also applied to study the bubble dynamic and bubble position inside the nozzle. A modified form of critical pressure was also used to evaluate critical pressure as cavitation starts and showed critical pressure increases significantly as cavitation starts. The bubble shock wave due to the first and second bubble collapse was predicted in the cavitating and non-cavitating flow. A shock wave due to the bubble's first collapse in cavitation inception conditions increased to 28 Mpa. Results showed that increasing the pressure difference can severely increase the shockwave while increasing the initial radius will decrease the amount of the emitted shockwave. Effects of surface tension, dynamic viscosity, and liquid density on bubble dynamic were evaluated.

* Corresponding author: Tel.: +9821-22970052 ; Fax: +9821-22970052 ; E-mail address: M.mahdi@sru.ac.ir

1. Introduction

Cavitation is a phenomenon in which phase changes occur due to a sudden alteration in the amount of pressure while the temperature is constant. When the pressure decreases to less than the critical pressure, which is in some cases is equal to the vaporization pressure, cavitation occurs. Prediction of incipient cavitation is vital for nozzles (especially injector nozzle) since it can enhance atomization and reduce fuel impurities. Cavitation is observed in turbo pumps, hydrofoils, orifices, marine propellers, nozzles, venturies, pumps, flow channels, and turbines [1-10].

There are two approaches for two-phase flows: the Eulerian/Eulerian approach and the Eulerian/Lagrangian approach. In the Eulerian /Eulerian approach, two fluids are analyzed simultaneously, and in the Eulerian/Lagrangian approach, you have a continuum phase and another bubble phase. Several types of the Eulerian/Lagrangian approach have been used in many different studies. The trajectory and dynamic of the bubble can be determined by simultaneously solving the Rayleigh Plesset (RP) equation and the bubble equation of motion. A numerical simulation of cavitation was correlated by Meyer *et al.* [11]. They developed a computer code for statically modeling incipient cavitation using the RP equation coupled with bubble motion equations. Chahine pursued the dynamics of traveling incipient cavitation bubbles by allowing nucleus deformation through inviscid potential flow [12]. Kevin J. Farrell predicted nuclei trajectories over a 5.08 cm diameter Schiebe body with an Eulerian / Lagrangian approach [13]. He modeled bubble growth using the RP equation and then studied bubbles using Newton's second law to account for various forces applied to the bubble. F. Delale considered the effects of bubble nucleation on quasi-one-dimensional steady-state cavitating nozzle flow [14]. The classical form of the RP equation and the polytropic law for partial gas pressure was used in their model. An Eulerian / Lagrangian computational approach was also used by Zhang and Ahmadi to simulate gas-liquid-solid flow [15]. In their assumption, bubble liquid and particles were considered in a two-way interaction. The bubble dynamic around NACA 0015 was investigated by Mahdi *et al.* [16]. Slip velocity between bubble and liquid was considered accurately in their model. Giannadakis *et al.* followed an Eulerian/Lagrangian approach to consider bubble breakup,

coalescence, and turbulent and turbulent dispersion for the first time in a cavitating flow inside a single hole injector nozzle [17]. The RP equation was also used in their simulations to consider bubble dynamics. They successfully modeled several aspects of cavitation, such as cavitation onset and super cavitation. Ochia *et al.* used an Eulerian/Lagrangian reference for predicting cavitation erosion in a cavitating flow [18]. They first simulated the cavitating flow using the equation of state of a two-phase medium. Afterwards, the energy of the bubble collapse was calculated by considering bubble dynamics through a Lagrangian frame, which led to surface erosion.

In this study, for the first time, a code is developed for calculating bubble dynamics inside a nozzle using a modified form of the RP equation and the equation of bubble motion with an Eulerian/Lagrangian approach. Since the focus of this paper is on the Lagrangian phase, the Eulerian equation will be briefly mentioned. Eulerian and Lagrangian approaches will be illustrated in more detail in the subsequent sections, and the bubble collapse region and emitted shock wave from the bubble are comprehensively illustrated in cavitating and non-cavitating flow regimes. We also used an Eulerian-Lagrangian approach from our previous publication on the main forces exerted on a spherical bubble during its motion inside a diesel injector nozzle [1].

The collapse of a bubble or cluster of bubbles can create a very significant wave that can be extremely harmful, especially solid surfaces, due to its sudden intense emitted wave. It is a very complex process to predict this phenomenon because the wave is very powerful and occurs instantly. Shockwaves have never been calculated inside diesel injector nozzles, and for the first time in this study, a comprehensive code is developed for the thorough investigation of bubble behavior inside diesel injector nozzles.

The effect of shockwaves on systems of biological relevance has been investigated by the primary Rayleigh-Plesset equation [19]. This thesis found that pressure excitation, which can make the bubble more active, can also cause cell damage along with transient membrane permeabilization. He also concluded that shock wave adherent cells in vitro can permeabilize the action of cavitation bubbles. Shock emission due to spherical bubble collapse in sulfuric acid had also been investigated in one of our previous publications [20]. In that study, the Gilmore equation for calculating bubble

dynamic and a set of Navier-Stokes equations for the gas inside the bubble were compared considering heat transfer, outward traveling shockwave strength, and velocity. It was concluded that the bubble center temperature, pressure, and maximum bubble wall velocity due to the amplitude of the acoustic field increases and bubble radius decreases. Finally, in this paper, the shockwave due to the first and second bubble collapse inside a diesel injector nozzle will be investigated and then compared.

2. Numerical method

In this study, a one-way coupling between the Eulerian and Lagrangian part is used, the numerical procedure is as follows:

- 1- Calculating the main flow field by the Eulerian approach for the whole computational domain (one-way coupling is used);
- 2- Determining the bubble dynamics and bubble trajectory (using pressure and velocity obtained from the Eulerian part of the Eulerian/Lagrangian approach for the whole computational domain);
- 3- Evaluating the bubble dynamics while cavitation starts;
- 4- Calculating the emitted shock wave as cavitation occurs.

2.1. Calculating flow field (Eulerian approach)

For an incompressible fluid flow, the equation of continuity and balance of momentum can be derived as follows.

$$\frac{\partial \bar{u}_i}{\partial x_i} = 0$$

$$\frac{\partial \bar{u}_i}{\partial t} + \bar{u}_j \frac{\partial \bar{u}_i}{\partial x_j} = -\frac{1}{\rho} \frac{\partial \bar{P}}{\partial x_i} + \nu \frac{\partial^2 \bar{u}_i}{\partial x_j \partial x_j} - \frac{\partial}{\partial x_j} R_{ij} \quad (1)$$

where \bar{u}_i is the mean velocity, x_i is the position, t is the time, \bar{P} is the mean pressure, ρ is the constant mass density, ν is the kinematic viscosity, and $R_{ij} = \bar{u}'_i \bar{u}'_j$ is the Reynolds stress tensor. Here, $u'_i = u_i - \bar{u}_i$ is the fluid fluctuation velocity component.

The RSTM account for differential transport equations for evaluation of the turbulence stress components, i.e.,

$$\frac{\partial}{\partial t} R_{ij} + \bar{u}_k \frac{\partial}{\partial x_k} R_{ij} = \frac{\partial}{\partial x_k} \left(\frac{\nu_t}{\sigma^k} R_{ij} \right) - \left[R_{jk} \frac{\partial \bar{u}_j}{\partial x_k} \right] - C_1 \frac{\epsilon}{k} \left[R_{ij} - \frac{2}{3} \delta_{ij} k \right] - C_2 \left[P_{ij} - \frac{2}{3} \delta_{ij} \epsilon_1 \right] \quad (2)$$

where the turbulence production terms can be determined is as in Eq. (3).

$$P_{ij} = -R_{jk} \frac{\partial \bar{u}_j}{\partial x_k} - R_{jk} \frac{\partial \bar{u}_i}{\partial x_k}$$

$$P = \frac{1}{2} P_{ij} \quad (3)$$

where is the fluctuation kinetic energy production. ν_t is the turbulent viscosity. And, finally, $\sigma^k=1.0$, $C_1=1.8$, and $C_2 = 0.6$ are empirical constants. ϵ , which is the turbulent dissipation rate, is computed from the Eq. (4).

$$\frac{\partial \epsilon}{\partial t} + \bar{u}_j \frac{\partial \epsilon}{\partial x_j} = \frac{\partial}{\partial x_i} \left[\left(\nu + \frac{\nu_t}{\sigma^\epsilon} \right) \frac{\partial \epsilon}{\partial x_i} \right] - C^{\epsilon 1} \frac{\epsilon}{k} R_{ij} \frac{\partial u_i}{\partial x_j} - C^{\epsilon 2} \frac{\epsilon^2}{k} \quad (4)$$

In Eqs. (2) and (4), $k = \frac{1}{2} \bar{u}'_i \bar{u}'_i$ is the fluctuation kinetic energy and ϵ is the turbulent dissipation. The constant values are as follows [21,22].

$$\sigma^k=1.3, C^{\epsilon 1}=1.44, C^{\epsilon 2}=1.92 \quad (5)$$

The flow field was analyzed using incompressible RANS equations and the finite volume method. The Reynolds stress transport model (RStM), developed by Launder *et al.* [21], was used to determine the turbulent parameters, such as turbulent kinetic energy and turbulent dissipation rate. By determining turbulent parameters with RStM, the fluctuating components of velocity cannot be calculated. The continuous filter white noise (CFWN), modified and applied by Shams and Ahmadi [22], was used to generate the instantaneous fluctuating components of fluid velocity. Instantaneous fluid velocity can be calculated using Eq. (6).

$$\frac{du_i}{dt} = -\frac{u_i - \bar{u}_i}{T_i} + \left(\frac{2\bar{u}'^2}{T_i} \right) \xi_i(t) \quad (6)$$

In Eq. (6), u_i is the fluctuating term of velocity in each direction, \bar{u}_i is the mean flow velocity in each direction, \bar{u}'^2 is the mean square of fluctuating components of velocity, and $\xi_i(t)$ is a Gaussian vector white noise random process. In Eq. (6) T_i is the particle integral

time, which can be defined as average time that is spent in turbulent eddies along the particle path, is as follows:

$$T_I = \int_0^\infty \frac{u'_p(t)u'_p(t+s)}{u'_qu'_q} ds \quad (7)$$

For a small particle that moves with the fluid, the particle integral time may be approximated by the fluid point Lagrangian integral time T_I . The latter parameter determines the relationship between fluctuation kinetic energy and dissipation rate, which can be calculated as follows:

$$T_I \approx C_L \frac{k}{\epsilon} \quad (8)$$

In Eq. (8), T_I is the average elapsed time of a particle in eddies during bubble motion. In Eq. (7), for $C_L \approx 0.3$ [23], k is the turbulent kinetic energy and ϵ is the turbulent dissipation rate. The term $\xi_i(t)$ in each time step can be calculated as follows:

$$\xi_i(t) = \frac{G_i}{\sqrt{\Delta t}} \quad (9)$$

where G_i is the independent Gaussian random number with zero mean and unit variance. Δt is the time step, which is variable in this study and varies according to the bubble radius variation. Fluctuating terms of velocity will be coupled with the Lagrangian solution for more accuracy. Solving the Eulerian approach is not complex as the RANS equations are solved in many textbooks and papers; thus, the main focus of this paper is on the Lagrangian approach.

2.2. Calculating bubble dynamic and trajectory (Lagrangian approach)

While the mean flow field and turbulent parameters are calculated through the Eulerian approach, the bubble dynamic and bubble trajectory should be determined for predicting incipient cavitation. A modified form of the RP equation developed by Loftsted *et al.* was used to calculate the bubble dynamics [24]. This model also considers the effects of compressibility as follows:

$$R\ddot{R} + \frac{3}{2}\dot{R}^2 = \frac{1}{\rho} \left[(P_g - P_0 - P_s) - 4\mu \frac{\dot{R}}{R} - 2\frac{\sigma}{R} + \frac{R}{c} \frac{d}{dt}(P_g) \right] \quad (10)$$

$$P_g(t) = (P_{g0}) \left(\frac{R_0}{R} \right)^{3\gamma} \quad (11)$$

$$P_{g0} = P_{inf} + 2\frac{\sigma}{R_0} - P_{cr} \quad (12)$$

In Eq. (10), R is the radius of the bubble in each time step, \dot{R} is the first time derivative of the bubble radius (bubble wall velocity), \ddot{R} is the second time derivative of the bubble radius, ρ is the density of the diesel fuel, $P_0 = 101325$ Pa, μ is the dynamic viscosity, σ is the surface tension, c is the speed of the sound, P_s is the pressure at the bubble surface, and P_g is the gas pressure inside the bubble. In Eq. (11), P_{g0} is the initial gas pressure inside the bubble, P_{cr} is the critical pressure, and γ is the polytropic gas constant. Since there is slip velocity between the bubble and carrying fuel, an additional term should be added to the RP equation, which is as follows [25]:

$$R\ddot{R} + \frac{3}{2}\dot{R}^2 = \frac{1}{\rho} \left[(P_g - P_0 - P_s) - 4\mu \frac{\dot{R}}{R} - 2\frac{\sigma}{R} + \frac{R}{c} \frac{d}{dt}(P_g) \right] + \frac{\rho(\vec{U} - \vec{U}_b)^2}{4} \quad (13)$$

In Eq. (13), the second term on the right side of the equation accounts for the effect of slip velocity, \vec{U} is the resultant velocity of the liquid in x and y directions, and \vec{U}_b is the resultant velocity of the bubble in x and y directions. Maxey *et al.* proposed an equation that was able to track bubble trajectory using the Lagrangian approach [18]. Using Newton's second law, forces applied to the bubble are considered. Saffman force is also added to Maxey equation for more accuracy. The modified form of Maxey equation for bubble motion is as follows:

$$\frac{dU_b}{dt} = 2g\vec{j} - \frac{3}{\rho} \nabla \bar{p} + \frac{3C_D}{4R} (\vec{U} - \vec{U}_b) |\vec{U} - \vec{U}_b| + \frac{3}{R} (\vec{U} - \vec{U}_b) \dot{R} + \frac{1.542}{R} \nu^{0.5} (\vec{U} - \vec{U}_b) \left| \frac{d\vec{U}}{dy} \right|^{0.5} \text{sgn} \left(\frac{d\vec{U}}{dy} \right) \vec{j} \quad (14)$$

In Eq. (14), g is the earth gravity, ν is the kinematic viscosity of the carrying liquid, and $\nabla \bar{p}$ is the pressure gradient in the area in which the bubble is located. C_D is the drag coefficient of the bubble, which can be determined according to Hagerman and Morton's empirical equation [26].

$$C_D = \frac{24}{Re} (1 - 0.197 Re^{0.63}) + \frac{24}{Re} (2.6 \times 10^{-4} Re^{1.38}) \quad (15)$$

$$Re = \frac{2R |U - U_b|}{\nu} \quad (16)$$

In Eq. (15), Re is the Reynolds number for relative velocity between the bubble and the carrying liquid. Eq. (14) should be separately rewritten in x and y directions. Afterwards, two ordinary differential equations (ODE) will appear. Eq. (13) is ODE as well. These three

second order ODEs are coupled with each other and can be solved by the fifth order Runge-Kutta (RK) method. The CFWN equation will be also coupled with RP and bubble motion equations.

2.3. Calculating critical pressure

Singhal *et al.* proposed a critical pressure for predicting cavitation more accurately [27]. In this model, the effect of pressure fluctuation is also considered on the critical pressure, which is shown in Eq. (17).

$$p_{cr} = p_v + \frac{1}{2}(0.39\rho k) \quad (17)$$

In Eq. (17), p_v is the vaporization pressure, ρ is the density of the carrying liquid, and k is the turbulent kinetic energy.

2.4. Calculating emitted shock wave from bubble collapse

When a bubble collapses, it induces a very significant amount of pressure called a shock wave (pressure wave). Gilmore calculated the amount of the pressure wave using the Kirkwood and Bethe hypothesis [28]. To evaluate the pressure wave, it is necessary to determine the characteristic curve and velocity field.

$$Y = \frac{R\dot{R}^2}{2} + \frac{R(P_s - P_{inf})}{\rho} \left(1 - \frac{(P_s - P_{inf})}{2\rho C^2}\right) \quad (18)$$

$$U_w = \frac{Y}{cr_{dist}} + \frac{\left(\frac{CR^2\dot{R}}{Y^2}\right)Y^2}{c^3r_{dist}^2} \left(1 - \frac{Y}{c^3r_{dist}} + \frac{\left(\frac{CR^2\dot{R}}{Y^2}\right)Y^4}{2c^8r_{dist}^4}\right) \quad (19)$$

In Eqs. (18) and (19), Y is the characteristic curve, P_s is the pressure at the bubble surface, P_{inf} is the infinity pressure (which is approximately atmospheric pressure), U_w is the emitted velocity wave from the bubble collapse, and r_{dist} is the radial distance from the bubble center. When the characteristic curve and velocity wave are calculated, the pressure wave can be calculated as in Eq. (20).

$$P_w = P_{inf} + \rho \left(\frac{Y}{r_{dist}} - \frac{U_w^2}{2}\right) + \frac{\rho}{2C^2} \left(\frac{Y}{r_{dist}} - \frac{U_w^2}{2}\right) \quad (20)$$

3. Calculation conditions

In this study, Winklhofer *et al.*'s J type nozzle was

used for the numerical simulation since it has robust experimental data for validation [29]. As represented in Fig. 1, the pressure boundary condition was used for the inlet and outlet pressure. No slip wall boundary condition was applied to the walls. The length of the inlet area was 1000 μm , and that of the outlet was 299 μm . The length of the orifice area was also 1000 μm . There was no contraction in the orifice area of the nozzle. A coordinate axis was placed in the inlet region of the nozzle. Diesel fuel properties were obtained from Altimira and Fuchs [5]. In all cases, the inlet pressure was 10 MPa. A simulation was performed for two cases. Case one, cavitation inception, was when cavitation started, and case two was the flow that had no cavitation. Cavitation started when outlet pressure reached 4.3 MPa, which is the boundary condition for the Eulerian approach. In the case with no cavitation, the outlet pressure was 6 MPa, which is the boundary condition for the Eulerian approach. Grid independence was checked in our previous publications [1,30-32]. The grid used in the present study was 74×44 in the orifice. The SIMPLE scheme was used to solve the pressure and momentum equations. Other solvers and discretization schemes are listed in Table 1. The convergence criteria for the residuals of all equations are set to 10^{-4} . The simulation procedure was done using a 2.26 GHz Intel(R) E5507 Quad-Core Processor (Core i7) with 16 GB of RAM running on a 64 bit Windows 8. Since the bubble was released near the entrance area of the orifice, the Lagrangian approach boundary conditions are as follows: $(R(0) = 0.4 \mu\text{m}$ (bubble initial radius), $dR/dt = \dot{R}(0) = 0 \text{ m.s}^{-1}$ (bubble wall velocity), $x(0) = 970$

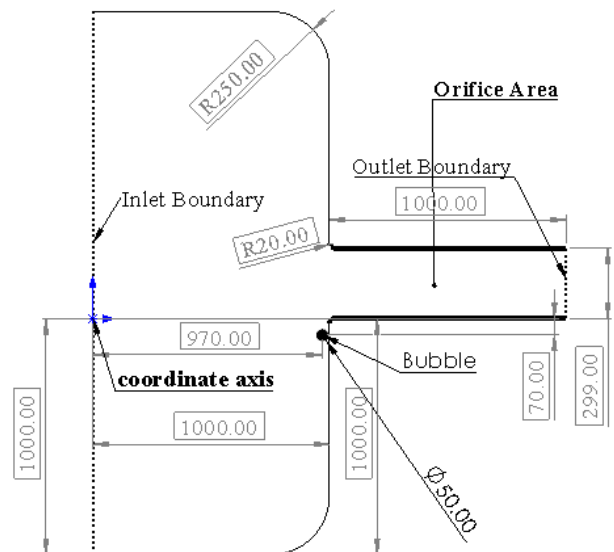


Fig. 1. Geometry of Winklhofer's J type nozzle.

Table 1. The chosen solver and discretization schemes.

Terms	Methods
Pressure-velocity Copling	SIMPLE
Gradient	Least Squares Cell Based
Discretization for Pressure	PRESTO!
Discretization for Volume Fraction	QUICK
Discretization for Momentum	Second Order Upwind
Discretization for K	Second Order Upwind
Discretization for ϵ	Second Order Upwind

μm (bubble initial x position), $y(0) = -70 \mu\text{m}$ (bubble initial y position), and $\dot{x}(0) = 1.7 \text{ m.s}^{-1}$, $\dot{y}(0) = 1.5 \text{ m.s}^{-1}$, where $\dot{x}(0)$ and $\dot{y}(0)$ are the initial bubble velocity in x and y directions). Also, Fig. 1 shows the exact position of the bubble released for the Lagrangian part. It is necessary to mention that the Eulerian part was solved steady, while the Lagrangian part was solved unsteady.

4. Results and discussion

Results were obtained from both the Eulerian and Lagrangian approaches. Since the main focus of this paper was on bubble dynamics and its pressure wave, the Eulerian approach was only briefly validated. Also, solving the RANS equation was not complex as many books and papers mention this solution.

4.1. Validation of numerical method

Winklhofer *et al.* reported pressure at the center line of the nozzle when back pressure is 3.5 MPa [29]. This regime is transitional from cavitation inception to super cavitation in the nozzle, which is called critical cavitation. Fig. 2 depicts that the pressure at the nozzle center line decreases significantly when flow enters the orifice inlet. According to this figure, when the bubble enters the orifice area of the nozzle, the pressure decreases immediately, which can lead to changes in the fluid behavior inside the nozzle. The presented numerical solution, which was the Eulerian approach toward the RANS equation, was able to predict the pressure profile at the nozzle center with good agreement with the experimental data.

Loftstedt *et al.* measured the dynamic behaviour of the bubble via sonoluminescence [23]. In this case, P_s in Eq. (4) can be written as follows:

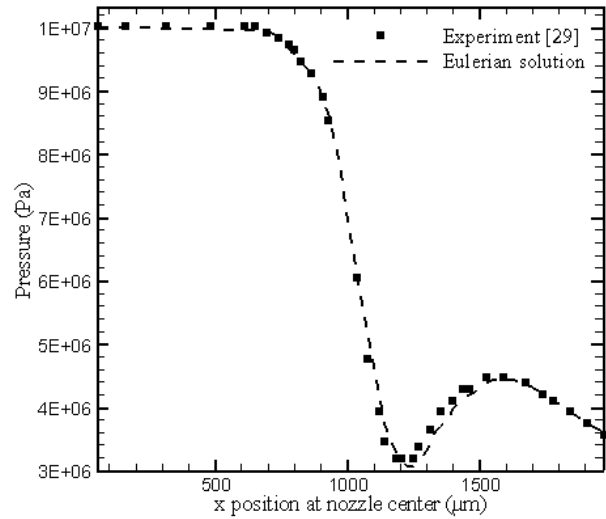


Fig. 2. Comparison of numerical and experimental data for pressure at the middle of nozzle.

$$P_s = P(t) = P_0 - P_A \sin \omega t \quad (21)$$

In Eq. (21), $P(t)$ is the sinusoidal driving pressure, $P_A = 1.35 \text{ bar}$ and $\omega = 26.5 \text{ KHz}$. In this case, in the first step, $R_0 = 4.5 \mu\text{m}$ and bubble wall velocity (\dot{R}) are zero. There are no experimental data for validating the RP equation for the flow inside the nozzle. Hence, the RP equation is validated using the experimental data obtained from the sonoluminescence phenomena. Fig. 3 shows bubble radius versus elapsed time as sonoluminescence occurs. This figure also indicates that the current numerical solution is able to predict the bubble collapse region (20.8 μs). The current numerical approach is able to predict the bubble peak radius according to the experimental data.

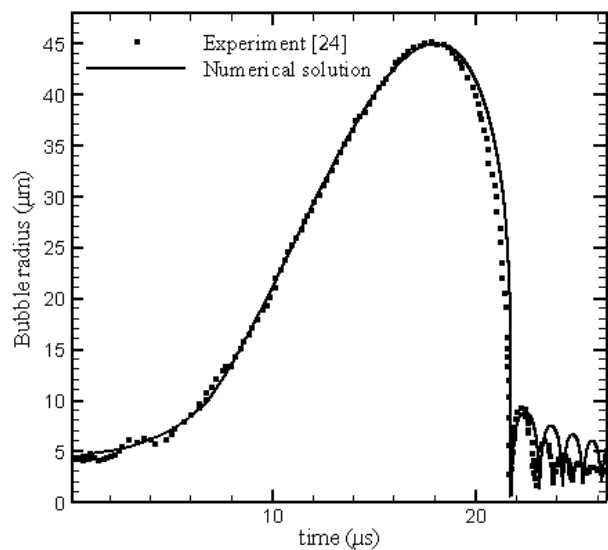


Fig. 3. Comparison of experimental and numerical data for the bubble radius in sonoluminescence.

4.2. Quantitative prediction of cavitation inception and its shock wave

The Eulerian approach was validated in the previous section. As mentioned before, the main flow field data are obtained through the Eulerian frame. Afterwards, the bubble should be released in the nozzle with the Lagrangian frame to calculate the dynamics of the bubble in cavitating and non-cavitating flows. All neighbourhood cells do not have equal distance to the bubble. During the bubble's motion inside the nozzle with the Lagrangian frame, some bubbles move very close to some cell centres; so, it seems to be necessary to define a criterion for the effects of neighbourhood cells on bubble properties. Fig. 4 is the main example of one time-step of bubble motion. As shown in Fig. 4, cell number 3 is the nearest cell to the bubble, while cell 2 is the farthest one from the bubble. According to the present criteria, the nearest cell has the highest portion in determining bubble properties, like velocity and pressure, during its motion inside the nozzle.

$$u_b = \frac{d_2 u_3 + d_3 u_1 + d_1 u_3 + d_4 u_2}{d_2 + d_3 + d_1 + d_4} \quad (22)$$

According to Eq. (16) and Fig. 4, bubble velocity (or pressure) can be obtained more accurately by considering the effect of neighborhood cells. In Eq. (22), subscripts 1 to 4 are related to cell 1 (C1), cell 2 (C2), cell 3 (C3), and cell 4 (C4), respectively. Eq. (22) can also be used for pressure by using p instead of u .

For solving Eq. (7), it is vital to determine the surface

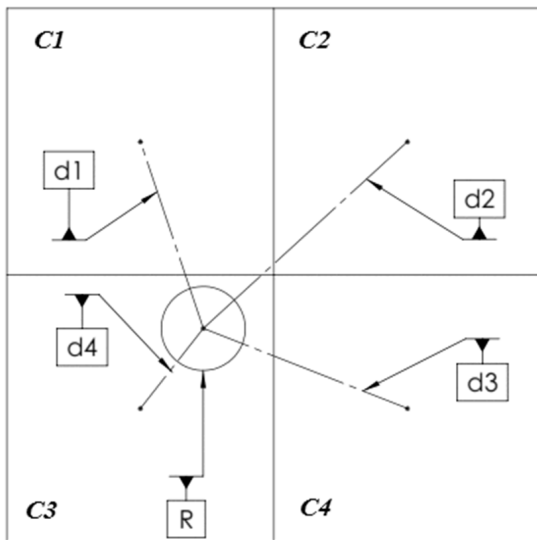


Fig. 4. The effect of neighborhood cell centers' on a bubble properties.

pressure of the bubble. After calculating the pressure at the center of the bubble with the procedure mentioned in Fig. 4 and Eq. (16), it is time to calculate the bubble surface pressure in each time step. As demonstrated in Fig. 5, bubble surface pressure can be determined by obtaining the bubble position of the bubble center (from the bubble motion equation) and the bubble radius (from the RP equation). First, six points with equal radial distances from each other are selected on the bubble surface. Then, by numerical formulation (Eq. (16)), the value of the pressure at each of these six points is calculated. Finally, by averaging these six values, the pressure at the bubble surface is determined. In the orifice area of the orifice, different pressure gradients cause a steep pressure change on the bubble surface; so, it is highly crucial to average surface pressure for an accurate simulation.

Winklhofer *et al.* also predicted cavitation region by the vapor volume fraction region when inlet pressure was 10 MPa and back pressure was 4.3 MPa (cavitation inception) [29]. According to Fig. 6, cavitation starts at 60 μm from the orifice entrance and ends at 280 μm from the orifice entrance. According to Fig. 6, it can be inferred that the core of cavitation occurs at approximately 180 μm from the orifice entrance. According to Eqs. (13) and (14), the bubble radius and bubble position in x and y directions are functions of time. Fig. 7 shows the bubble radius versus (μm) elapsed time (μs) during bubble motion inside the nozzle. According to this figure, the bubble collapses at 1.85 μs . On the other hand, the collapse position of the bubble should be necessarily determined. According to Figs. 8 and 9, the x and y positions of the bubble can be determined by obtaining the corresponding time of the

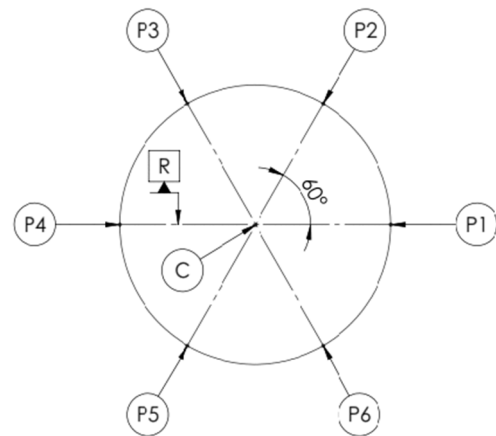


Fig. 5. Calculation of bubble surface pressure from bubble center pressure.

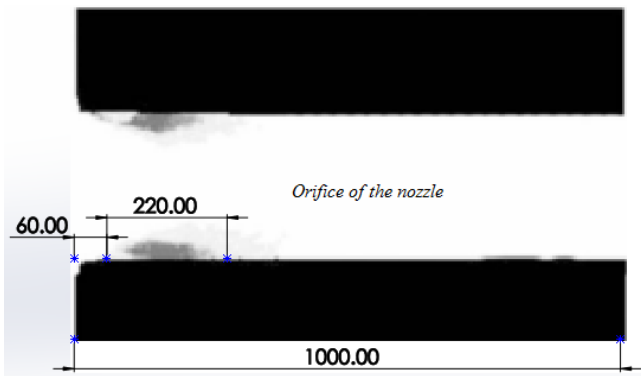


Fig. 6. Experimental data for the formation of cavitation inception by vapor volume fraction contour.

bubble inside the nozzle. From these two figures, it can be inferred that when the bubble collapses, its x position is 1200 μm from the coordinate axis (as seen in Fig. 1) and from the orifice entrance of the nozzle, which shows significant agreement with the experimental data (Fig. 4). Singhal *et al.* defined the vapor volume fraction as a function of bubble radius (R) and the number of bubble nuclei (n), which is as follows [25].

$$a = n \frac{4}{3} \pi R^3 \quad (23)$$

According to Eq. (23), which is for calculating vapor volume fraction (α), bubble radius is the most important reason for changing the amount of vapor volume fraction since the number of bubble nuclei is assumed to be constant in many simulations. Hence, when bubble radius increases, it is anticipated that vapor volume fraction also increases. According to Figs. 7 and 9, the bubble radius increases as much as 10 times from its initial radius when it enters the cavitating zone. In the non-cavitating regime (Fig. 7(a)), the bubble experiences no significant change compared with the cavitating regime. Fig. 7(b) is a close-up view of the circle in Fig. 7(a). According to this figure, the

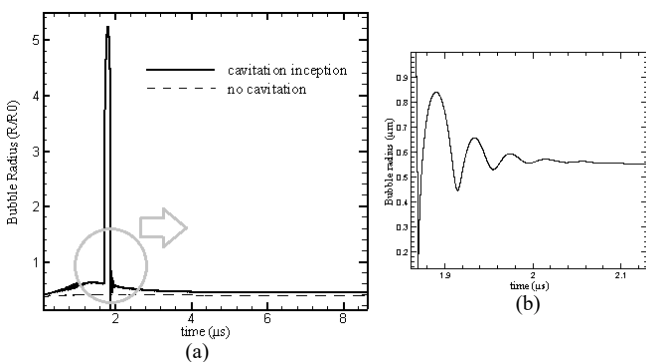


Fig. 7. (a) Change of bubble radius inside the nozzle for cavitating and non-cavitating regimes. (b) Collapse of bubble after growth.

second-highest value is obtained by the bubble radius of 0.85 μm , which is approximately one-seventh of the first highest value of the bubble radius. The ratio of the first highest value and the second-highest value of the bubble radius is called the damping factor. When the bubble radius damps to one-seventh of its radius, it shows that there is a significant loss of energy, which is more likely to be emitted as a shock wave (pressure wave), as will be discussed. Fig. 9 shows the y position versus elapsed time for the bubble inside the nozzle. According to this figure, the y position of the bubble changes steeply (circle) at 1.85 μs (collapse time). As is clear, the slope of Fig. 9 is the bubble velocity in y direction and increases when the y position of the bubble becomes vertical (circle). So, it can be inferred that the velocity of the bubble in y direction can also be used as a criterion for determining the region of bubble collapse and cavitation inception. On the other hand, entry into

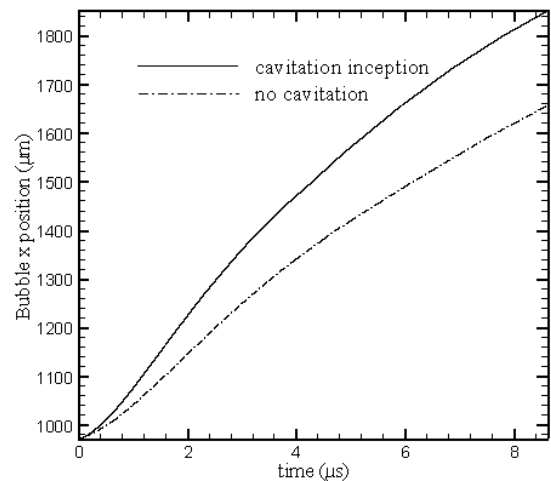


Fig. 8. Position of bubble in the x direction for cavitation and non-cavitating regimes.

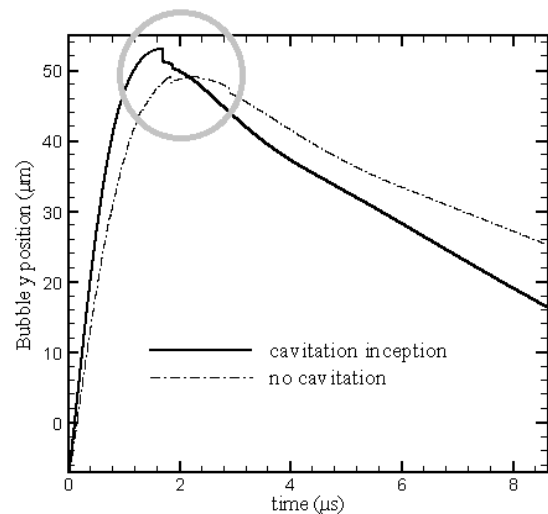


Fig. 9. Position of bubble in the y direction for cavitation and non-cavitating regimes.

the orifice formation of the recirculation region makes the bubble have a half orbital motion. According to Fig. 9, the bubble has fragmentary orbital motion around the inlet area of the orifice, which can make a re-entrant jet.

Traditionally, cavitation occurs when the local pressure of the fluid becomes less than the critical pressure. This critical pressure can be equal to the vaporization pressure in some cases but is not usually equal to the vaporization pressure. In this study, the formulation proposed by Singhal *et al.* was used [26]. This criterion also accounts for the effect of pressure fluctuation, which is mainly a function of turbulent fluctuation. Fig. 10 shows the bubble wall velocity versus elapsed time inside the orifice of the nozzle from the orifice entrance to the nozzle outlet. According to this figure, by the time that cavitation occurs, $1.6 - 2 \mu\text{s}$ the bubble wall radius changes immensely (cavitation area is shown inside the circle in Fig. 10), which can be due to the abrupt change in bubble radius, bubble y position, and swift changes in the pressure field. Fig. 11 shows critical pressure versus elapsed time in the case that cavitation inception occurs. This figure shows that the critical pressure of the fluid fluctuates in the position of the bubble. It reaches its highest value at $1.85 \mu\text{s}$, which is exactly the time that the bubble starts to grow (Fig. 7). The value of critical pressure in some time steps becomes extremely high. It reaches 0.27 MPa when cavitation starts, which is much higher than the vaporization pressure of diesel fuel ($p_v = 300 \text{ Pa}$).

According to Fig. 7, bubble wall velocity can be determined by (dR/dt) , which is the slope of the bubble radius line and is extremely high when the bubble

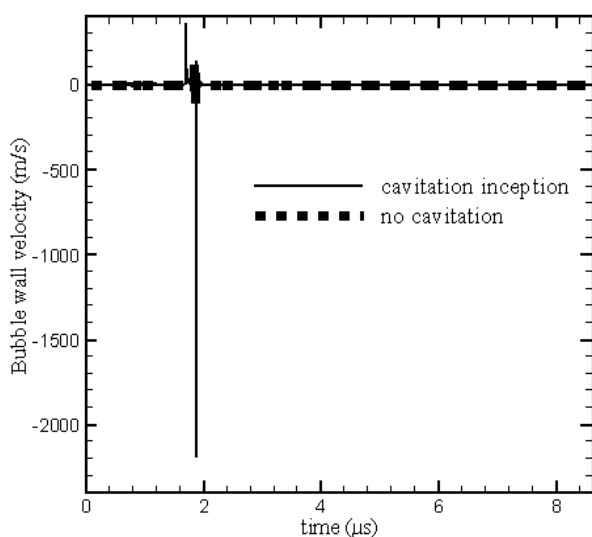


Fig. 10. Bubble wall velocity versus elapsed time.

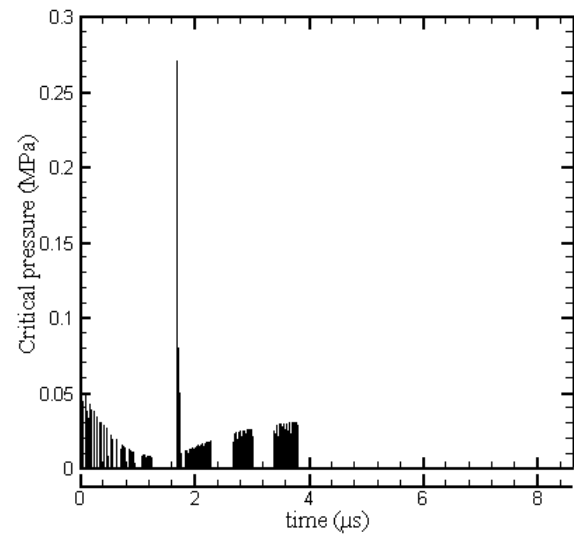


Fig. 11. The bubble's critical pressure when cavitation inception occurs.

collapse occurs. The collapse of the bubble can be very harmful since it makes an intense shock inside the carrying liquid, which is called a shock wave or pressure wave. Emitting a shock wave can also change the fuel behavior inside the nozzle since it occurs instantaneously. Fig. 12 shows the emitted shock wave versus radial distance from the bubble center in cavitating and non-cavitating flow regimes. Distance from the bubble center is approximately the distance from the collapse position of the bubble inside the nozzle. According to Fig. 12, the collapse of the bubble in the cavitating flow emits a shock wave that reaches 28 MPa . On the other hand, in the non-cavitating flow regime, the shock wave reaches 6 MPa , which is remarkably less than the value of the shock wave in the cavitating flow. According to Fig. 12, the shock wave

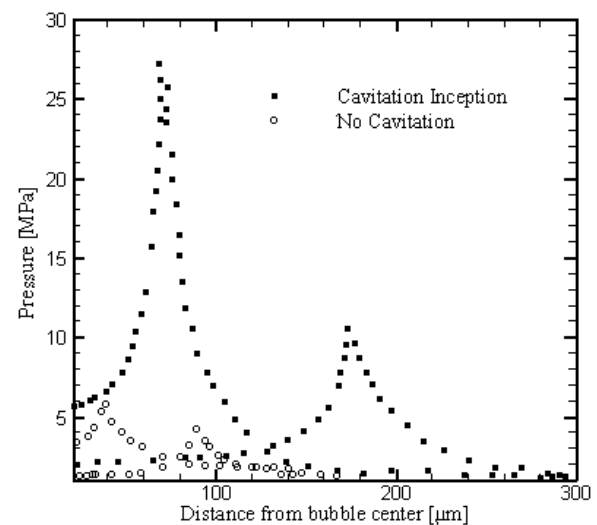


Fig. 12. Emitted shock wave from bubble collapse for cavitating and non-cavitating regimes

reaches its highest value at 30 μm from the collapse region of the bubble. The second collapse of the bubble is less intense and emits 11 MPa, which is sharply less than its corresponding value in the first collapse. This huge difference between the highest amounts of shock waves in the cavitating flow can be due to the radius change and high ratio of damping inside the nozzle. As mentioned before, the second-highest radius reached by the bubble is one-seventh of the first highest radius obtained by the bubble. It can be inferred that a higher amount of damping ratio for the bubble radius inside the nozzle leads to a remarkable difference between the amount of emitted shock wave from the first and second bubble collapse.

As mentioned in the previous section, the collapse of the bubble can emit several shockwaves in which the first shockwave is the most powerful. Therefore, in the subsequent sections, only the first shockwave will be mentioned. Fig. 13 shows the magnitude of the shockwave versus distance from the bubble center in different values of pressure difference. In this study, $R_0 = 0.4 \mu\text{m}$ was used in all of the simulations, and Fig. 13 depicts that increasing the amount of initial radius can significantly change the shape of the shockwave. In other words, increasing initial velocity can make a shockwave to be more bell shaped. All in all, increasing the initial radius of the bubble can decrease the amount of shockwave, which shows that bubbles with a small initial radius are more dangerous due to the larger shockwave that they can release.

In this study, cavitation inception occurs when the pressure difference is 60 MPa, and super cavitation

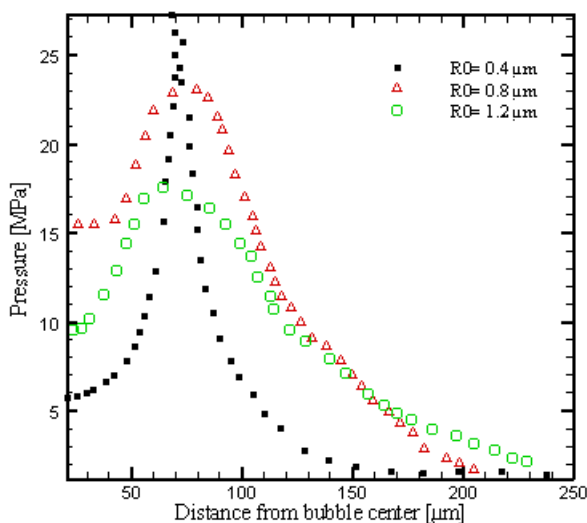


Fig. 13. Emitted bubble shockwave when different initial radii were used.

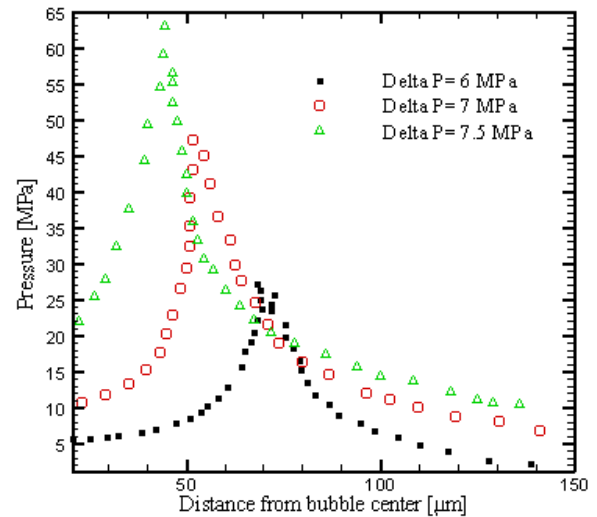


Fig. 14. Emitted bubble shockwave when different pressure differences were used.

occurs when the pressure difference is 75 MPa. According to Fig. 14, increasing the amount of shockwave can intensely increase the maximum value of shockwave. As Fig. 14 shows, increasing the pressure difference from 6 to 7.5 MPa can increase the amount of shockwave intensely, which can cause severe erosion of the surface of the orifice. This code is able to predict the exact location of the bubble collapse, which can be helpful to overcome the negative effects of the shockwave. If more resistant materials, which are more expensive, can be used in susceptible regions where the bubble collapse is more severe, it is possible to increase the life cycle of the orifice of injectors.

4.3. Effects of liquid properties on bubble dynamic and emitted shockwave

As liquid changes, the dynamics of the bubble changes as well. Different liquids have different properties and different effects on bubble dynamics. In this section, three main constants, density, dynamic viscosity, and surface, are changed in order to evaluate the effects of each constant on bubble behavior and dynamics. Several simulations were performed to calculate the effects of these three constants.

Table 2 shows the bubble radius and position of the bubble collapse when the three constants of the liquid change. Among these three constants, surface tension (s) has the most intense effect on the maximum bubble radius and position of the bubble collapse. When the surface tension increases by 25%, the bubble maximum pressure increases by 14%, and its collapse position

Table 2. Effects of liquid properties on bubble dynamics.

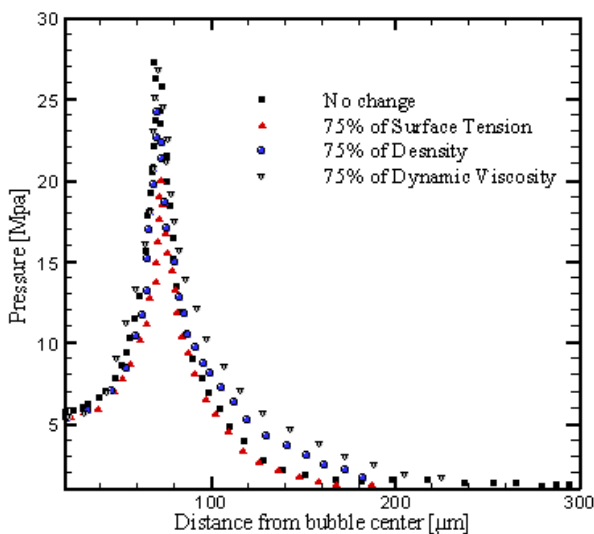
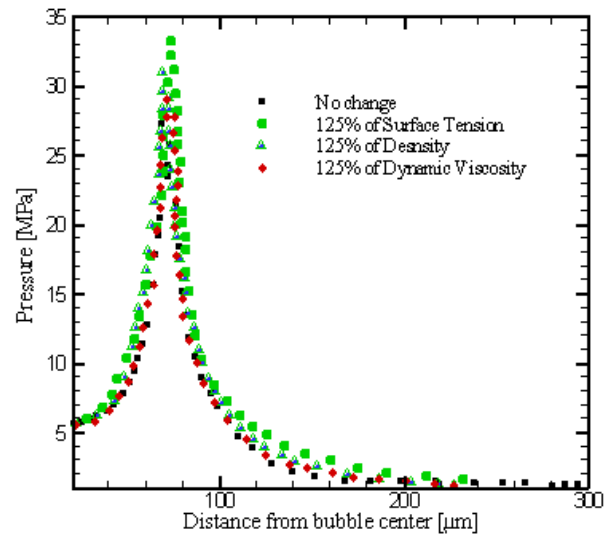
	Maximum bubble radius (μm)	Bubble collapse position (μm)
μ	5.236e-6	1204.6e
1.25 μ	5.270e-6	1200.8e
0.75 μ	5.210e-6	1207.6e
s	5.236e-6	1204.6e
1.25 s	5.963e-6	1082.0e
0.75 s	4.595e-6	1313.1e
ρ	5.236e-6	1204.6e
1.25 ρ	5.617e-6	1208.5e
0.75 ρ	4.911e-6	1201.7e

moves closer to the orifice inlet. On the other hand, since RP is a nonlinear equation, decreasing the surface tension by 25% decreases the bubble's maximum radius by 12.3%, and its position moves closer to the orifice outlet by 9%. So, increasing and decreasing parameters do not have the same effects. Amazingly, the density of liquid (ρ) has an intense effect on the bubble radius and a trivial effect on the position of the bubble collapse. Finally, the dynamic viscosity of the liquid has a minor effect on the maximum bubble radius and bubble collapse position. Increasing or decreasing dynamic viscosity by 25% changes the bubble maximum radius by less than 1%. Using fluids with higher surface tension and density can increase maximum bubble radius and could also emit more shock waves since as the maximum bubble radius increases, the damping ratio will also be increased.

Fig. 15 shows the magnitude of the shockwave as density (ρ), surface tension (σ), and dynamic viscosity

(μ), each of which decreased by 25%. In other words, we decreased the amount of the three mentioned parameters in the Eulerian part of the equation and solved it with new pressure and velocity values obtained from the Lagrangian part of the current study. Fig. 15 shows that decreasing dynamic viscosity by 25% will not significantly change the value of the shockwave, but decreasing the surface tension in the Eulerian part can significantly decrease the value of the shockwave. Decreasing all three parameters can decrease the maximum value of the shockwave, and the effect of the surface is the most notable. Fig. 16 also shows the magnitude of the shockwave, as ρ , σ and μ , also each increased by 25% in the Eulerian part. After obtaining the pressure and velocity in all computations in the Eulerian part, a simulation in the Lagrangian part was performed, which shows that increasing dynamic viscosity did not change the value of the shockwave, but increasing the surface tension increased the shockwave up to 15%.

Fig. 17 shows the bubble center pressure versus initial bubble radius as the pressure difference varies from 6 to 7.5 MPa. According to Fig. 17, increasing the initial radius of the bubble radius can decrease bubble center pressure. As the pressure difference also increases, the decrease in the value of the bubble center pressure caused by increasing the initial radius of the bubble is more severe. When the pressure difference is 6 MPa, increasing the initial radius of the bubble does not change the bubble center pressure significantly but increasing the pressure difference to 7.5 MPa can decrease the shockwave as the initial bubble radius

**Fig. 15.** Emitted bubble shockwave as surface tension, dynamic viscosity, and density decreased by 25%.**Fig. 16.** Emitted bubble shockwave as surface tension, dynamic viscosity, and density increased by 25%.

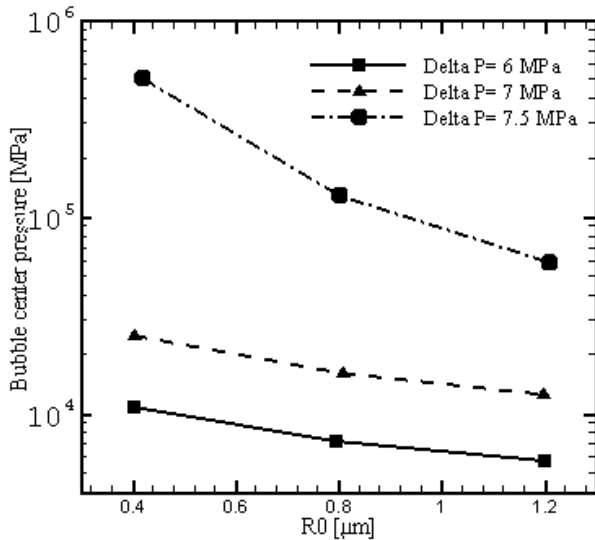


Fig. 17. Bubble center pressure versus initial radius of bubble as pressure difference changes.

increases. Finally, Fig. 18 shows the maximum bubble wall velocity versus the initial bubble radius as pressure changes. According to Fig. 18, increasing the pressure difference from 6 to 7.5 MPa can cause the bubble radius to change from 2200 to 3800 m.s⁻¹, which is remarkable. Also, increasing the initial radius of the bubble can decrease the maximum bubble wall velocity.

5. Conclusion

In the present study, an Eulerian approach using RANS equations with a finite volume scheme was used. RSTM was used to calculate turbulent parameters. The CFWN model was also employed for calculating fluctuating terms of the velocity. After obtaining pressure and velocity from the Eulerian simulation (one coupling was employed), the dynamics of a bubble were accurately calculated with the Lagrangian frame and variable time step using the RP equation and equation of bubble motion. Experimental data from Winkhofer *et al.* [29] and Losftstedt *et al.* [24] were used to validate the Eulerian simulation of carrying liquid and the Lagrangian simulation of bubble dynamic, respectively. According to the current criteria, cavitation inception was successfully predicted. The effect of liquid constants on bubble dynamic was investigated, and the emitted shock wave from the bubble collapse was also calculated. Cavitation occurred when the bubble radius inside the carrying liquid increased; after bubble growth, it collapsed, and the bubble collapse induced a significant shock wave inside the nozzle. The main

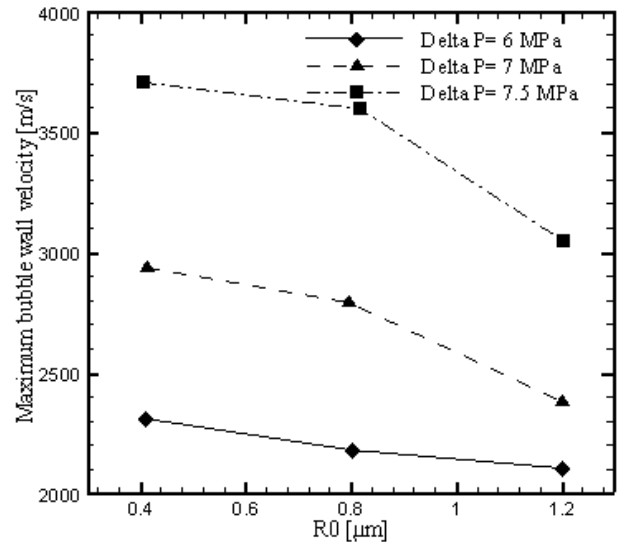


Fig. 18. Maximum bubble wall velocity versus initial radius of bubble as pressure difference changes.

results can be summarized as follows:

1. Bubble radius increased enormously as cavitation started, and there were no significant changes in the amount of bubble radius in the non-cavitating condition. Thus, the present numerical code was able to predict cavitation inception inside the nozzle since vast differences in bubble's behavior in the area where cavitation was observed in experiment data by Winklhofer *et al.* [29] can be observed.
2. Critical pressure, proposed by Singhal *et al.* [27] increased when cavitation occurred at 0.27 MPa, showing that the turbulent kinetic energy became intense in the cavitating flow as cavitation started due to abrupt, chaotic changes in the flow characteristics.
3. The velocity of the bubble in the y direction can be used as a criterion for bubble collapse since it became extremely high as the bubble collapsed.
4. Bubble collapse in the cavitating regime propagated a shockwave, which was approximately 28 MPa, and could be extremely harmful to the nozzle's surface. On the other hand, the second bubble collapse did not emit a noticeable amount of shockwave. In the non-cavitating flow, there was no immense amount of shock wave.
5. Increasing the pressure difference can significantly increase the amount of the emitted shockwave. In other words, increasing the pressure difference from 6 to 7.5 MPa can increase the shockwave by more than two times. On the other hand, increasing the initial radius of the bubble will decrease the shockwave and also can make the shockwave to be bell shaped.

6. Surface tension had an intense effect on bubble dynamics (maximum bubble radius) and the collapse position of the bubble. Liquid density had a considerably large effect on the bubble radius; but, it had a minor effect on the position of the bubble collapse. Liquid dynamic viscosity had a trivial effect on the bubble dynamic. Also, increasing the three mentioned parameters by 25% increased the shockwave. Interestingly, the amount of increase in the shockwave when surface tension increases by 25% was much higher than when the dynamic viscosity increased by 25%. Moreover, decreasing the three mentioned parameters by 25% can decrease the bubble shockwave.

References

- [1] S.M.J. Zeidi, M. Mahdi, Evaluation of the physical forces exerted on a spherical bubble inside the nozzle in a cavitating flow with an Eulerian/Lagrangian approach, *Eur. J. of Phys.* 136 (2015) 065041.
- [2] D. Schmidt, M. Corradini, The internal flow of diesel fuel injector nozzles: A review, *Int. J. Engine Res.* 2 (2001) 1-22.
- [3] S. Malavasi, V.M. Gianandrea, Dissipation and cavitation characteristics of single-hole orifices, *J. Fluids Eng.* 133 (2011) 051302.
- [4] D.P. Schmidt, Cavitation in diesel fuel injector nozzles, PhD thesis, University of Wisconsin Madison, 1997.
- [5] M. Altimira, L. Fuchs, Numerical investigation of throttle flow under cavitating conditions, *Int. J. Multiphas. Flow*, 75 (2015) 124-136.
- [6] A. Sou, B. Bicer, A. Tomiyama, Numerical simulation of incipient cavitation flow in a nozzle of fuel injector, *Comput. Fluids*, 103 (2014) 42-48.
- [7] Q. Xue, M. Battistoni, C.F. Powell, D.E. Longman, S.P. Quan, E. Pomraning, P.K. Senecal, P.D. Schmid, S. Som, An Eulerian CFD model and X-ray radiography for coupled nozzle flow and spray in internal combustion engines, *Intl. J. Multiphas. Flow*, 70 (2015) 77-88.
- [8] F.J. Salvador, M. Carreres, D. Jaramillo, J. Martínez-López, Comparison of microsac and VCO diesel injector nozzles in terms of internal nozzle flow characteristics, *Energ. Convers. Manage.* 103 (2015) 284-299.
- [9] T. Chien-Chou, W. Li-Jie, Investigations of empirical coefficients of cavitation and turbulence model through steady and unsteady turbulent cavitating flows, *Comput. Fluids*, 103 (2014) 262-274.
- [10] D.P. Schmidt, Theoretical analysis for achieving high-order spatial accuracy in Lagrangian/Eulerian source terms, *Int. J. Numer. Meth. Fl.* 52 (2006) 843-865.
- [11] R.S. Meyer, M.L. Billet, J.W. Holl, Freestream nuclei and traveling-bubble cavitation, *J. Fluid. Eng.* 114 (1992) 672-679.
- [12] G.L. Chahine, Numerical Simulation of Cavitation Dynamics, Dynaflow, Inc., Maryland, USA, 1997.
- [13] K.J. Farrell, Eulerian/Lagrangian analysis for the prediction of cavitation inception, *J. Fluid. Eng.* 125 (2003) 46-52.
- [14] C.F. Delale, Steady-state cavitating nozzle flows with nucleation, Fifth International Symposium on Cavitation, Osaka, Japan, 2003.
- [15] X. Zhang, G. Ahmadi, Eulerian-Lagrangian simulations of liquid-gas-solid flows in three-phase slurry reactors, *Chem. Eng. Sci.* 60 (2005) 5091-5106.
- [16] M. Mahdi, M. Shams, R. Ebrahimi, Numerical simulation of scaling effect on bubble dynamic in turbulent flow around hydrofoil, *J. Aerospace Sci. Tech.* 3 (2006) 67-75.
- [17] E. Giannadakis, M. Gavaises, C. Arcoumanis, Modelling of cavitation in diesel injector nozzles, *J. Fluid Mech.* 616 (2008) 153-193.
- [18] N. Ochiai, Y. Iga, M. Nohmi, T. Ikohagi, Study of quantitative numerical prediction of cavitation erosion in cavitating flow, *J. Fluid Eng.* 135 (2013) 011302.
- [19] B. Wolfrum, Cavitation and shock wave effects on biological systems, PhD thesis, Universität zu Göttingen, 2004.
- [20] M. Mahdi, M. Shams, R. Ebrahimi, Effects of heat transfer on the strength of shock waves emitted upon spherical bubble collapse, *Int. J. Numer. Method H.* 20 (2009) 372-391.
- [21] B.F. Launder, G.J. Reece, Progress in the development of a Reynolds stress turbulent closure, *J. Fluid Mech.* 68 (1975) 537-566.
- [22] M. Shams, G. Ahmadi, Computational modeling of flow and sediment transport and deposition in meandering rivers, *Adv. Water Resour.* 25 (2002) 689-699.
- [23] B.J. Daly, F.H. Harlow, Transport equation in turbulence, *Aerosol Sci. Tech.* 11 (1970) 133-143.

- [24] R. Lofstedt, B.P. Burber, S.J. Putterman, Toward a hydrodynamic theory of sonoluminescence, *Phys. Fluids*, 5 (1993) 2911.
- [25] C.T. Hsiao, G. Chorine, Prediction of vortex cavitation inception using coupled spherical non-spherical models and UnRANS computations, 24th Symposium on Naval Hydrodynamics, Fukooka, Japan, 2002.
- [26] M.R. Maxey, J.J. Riley, Equation of motion for a small rigid sphere in a nonuniform flow, *Phys. Fluids*, 26 (1983) 883-889.
- [27] A.K. Singhal, M.M. Athavale, H. Li, Y. Jiang, Mathematical basis and validation of the full cavitation model, *J. Fluid Eng.* 124 (2002) 617-624.
- [28] F.R. Gilmore, Hydrodynamic Laboratory Report 26.4, California Institute of Technology, Pasadena, CA, 1956.
- [29] E. Winklhofer, E. Kull, E. Kelz, A. Morozov, Comprehensive hydraulic and flow field documentation in model throttle experiments under cavitation conditions, Proc. of the ILASS-Europe Conference, Zurich, 2001.
- [30] S.M.J. Zeidi, M. Mahdi, Investigation effects of injection pressure and compressibility and nozzle entry in diesel injector nozzle's flow, *J. Appl. Comput. Mech.* 2 (2015) 83-94.
- [31] S.M.J. Zeidi, M. Mahdi, Effects of nozzle geometry and fuel characteristics on cavitation phenomena in injection nozzles, The 22nd Annual International Conference on Mechanical Engineering-ISME2014, Tehran, Iran, 2014.
- [32] S.M.J. Zeidi, M. Mahdi, Investigation of viscosity effect on velocity profile and cavitation formation in diesel injector nozzle, Proceedings of the 8th International Conference on Internal Combustion Engines, Tehran, Iran, 2014.